High Rate Compressive Behaviour of a Dilatant Polymeric Foam

Kapil Bharadwaj Bhagavathula[1] · Austin Azar[1] · Simon Ouellet[2] · Sikhanda Satapathy[3] · Christopher R. Dennison[1] · James David Hogan[1]

Abstract

Polymeric foams are an essential part of personal protection equipment, such as helmets and body armor. In this work, the authors study the strain-rate dependent behavior of a dilatant polymeric foam, focusing on developing characterization and testing methodologies needed to better understand the links between microstructure and failure in these materials. The authors study these links for a commercially-available shear-thickening foam, named D3O LITE D. Prior to testing, the pore sizes (82 ± 26 μm), ligament thickness between pores (5–12 μm), and porosity ($83 \pm 5\%$) were quantified using scanning electron microscope images. Samples were then tested in compression under quasi-static conditions for a strain rate of 0.04 s^{-1} using an MTS testing apparatus, and in dynamic conditions using a split Hopkinson pressure bar apparatus for strain rates of 5280–5720 s^{-1}. For both rates, strains upwards of 85% were achieved and this allowed us to examine a variety of material failure behaviors, including elastic collapse, localization, pore collapse, densification and post pore collapse hardening. These mechanisms are observed in-situ during compression experiments using high-speed photography, and linked back to stress–strain responses of the materials. In this material, the elastic collapse stress for quasi-static and dynamic compression conditions was found to be 120 ± 40 kPa and 243 ± 47 kPa, respectively, and elastic modulus were noted of 2.4 ± 0.7 MPa and 3.8 ± 1.2 MPa, respectively. Following the elastic collapse, some unique specimen-scale localization features were observed during the dynamic experiments. These features are unique to dynamic compression and were not observed for the quasi-static case, demonstrating a demonstrating a distinct high-rate behavior for this material, possibly linked to its "shear thickening" label. After densification, complete pore collapse followed by post pore collapse hardening were observed for both strain rates. These results represent some of the first studies on shear-thickening foams in the literature, and the testing methodologies developed in this study will serve as the foundation for additional experimental and computation studies across a broader range of foam materials.

Keywords Material behaviour · Shear thickening foam · High strain-rate · Kolsky bar · Dynamic compression · Ultra high-speed photography

Introduction

The ability to dissipate energy using foams is an aspect that has many engineering challenges in dynamic applications, such as automotive industry [1], core materials in composite sandwich constructions [2], and personal protective equipment [3–5]. Typical foam materials used in these energy-absorbing applications include expanded polystyrene (EPS) [6–8], expanded polypropylene (EPP) [8, 9], and thermal polyurethanes (TPU) [3, 10]. These studies have focused on better understanding the effect of microstructure [9–11], density [8, 9, 11] and strain-rate [7, 9, 11–13] in tension [14] and compression [1, 6, 13–18], as well as during impact experiments using drop testing [19] and gas-gun approaches

✉ Kapil Bharadwaj Bhagavathula
bhagavat@ualberta.ca

✉ James David Hogan
jdhogan@ualberta.ca

[1] Department of Mechanical Engineering, The University of Alberta, Edmonton, AB T6G 2R3, Canada

[2] Valcartier Research Centre, Defence Research and Development Canada, Quebec, QC G3J1X5, Canada

[3] Soldier Protection Sciences Branch, U.S. Army Research Laboratory, Aberdeen Proving Ground, MD 21005, USA

[1]. In this paper, the authors investigate the rate-dependent compressive stress–strain response and failure of a polymeric foam, and so focus on presenting the limited literature in this area (specifically for the dynamic regime).

Split Hopkinson pressure bar (SHPB) is a widely recognized experimental technique used to investigate the strain-rate dependent response and stress–strain curves for a variety of soft engineering materials at high strain rates from 10^2 to 10^5 s^{-1} [2, 11, 13, 15, 20, 21]. For example, Saha et al. [11] have shown that different grades of rigid polyurethane (PUR) foams and cross-linked polyvinyl chloride (PVC) foams exhibit some form of strain rate dependency. At quasi-static strain rates, both PUR and PVC foams show an increase of ~15% in yield and peak stresses with every increase in one order of magnitude of the strain rates from 0.001 to 0.1 s^{-1}. At strain rates above 700 s^{-1}, they observed a twofold increase in the yield strengths, which were twice as much when compared to the quasi-static regime. They also observed that yield strengths remained constant with increasing strain rates up to 1700 s^{-1} and the only changes observed in the compressive response are at the peak stresses. Similarly, Ouellet et al. [13] performed studies at strain rates from 0.008 to 2700 s^{-1} and found that polystyrene foams exhibited noticeable strain rate dependency in stresses only at rates greater than 100 s^{-1}. Their paper also looked at polyethylene foams and found that these also exhibit rate dependency, but only at strains greater than 20%. In another paper, Song et al. [7] studied a different grade of polystyrene foam than Ouellet et al. [13] and found an increase of ~10% in collapse stress with every increase in the order of magnitude of the strain rates from 0.001 to 950 s^{-1}.

In many of these papers and other studies, the authors point to the importance of microstructure (usually in terms of density [9, 11, 19] and cell sizes [7, 9, 11]) and failure (usually through a post-test macroscopic assessment of the sample [8, 13, 22]) on the strain-rate dependent behavior of polymeric foams. For example, Di Landro et al. [6] and Santa Maria et al. [16] suggested smaller cell sizes results in increased strength compared to larger cell sizes. They also noted an increase in the amount of energy that was absorbed (through measure of strain energy) at higher strain rates for smaller cell sizes and, consequently, higher relative densities [6, 9, 11]. In addition to increases in strength and energy absorption behaviors for smaller cell sizes, Bouix et al. [9] found that smaller cell sizes resulted in less sensitivity to increasing strain rate when compared with larger cell sizes. The importance of cell sizes on the rate dependent behavior of polymeric foams is coupled to onset and evolution of failure processes in these materials, and how these processes compete at different strain rates (e.g., work by Saha et al. [11]). Several failure mechanisms that have been studied for polymeric forms are the inertia [22], stretching and buckling

of the cell walls [6], and the effects of trapped gases [6, 9]. Understanding these relationships between failure mechanisms, microstructure, and the strain-rate dependency of polymeric foams is important in order to develop improved materials in the future; this is what the authors begin to do in this paper.

Building upon these past works investigating effects of microstructure and failure on the strain-rate dependent behavior of polymeric foams, this paper investigates the high strain-rate deformation of dilatant foams that is advertised as "shear-thickening". This material is employed in both industrial and military applications where energy absorption qualities are desired. In this paper, the authors focus on characterizing the microstructure in terms of pore size and wall thickness and study compressive behavior of this shear-thickening foam for different strain rates. As limited work has been done in the published literature on shear thickening foam materials, this study intends to begin to establish an understanding of mechanical properties and dynamic behavior, accomplished through experimentation and characterization. The paper is comprised of the following sections: first, microstructure characterization techniques and sample preparation methods are established and described. Second, testing methods are presented, followed by the presentation of the experimental results. These results are supported by stress–strain curves and video images obtained from high-speed cameras. Finally, implications and contributions of this work are highlighted, and future directions are suggested.

Materials and Characterization

Material and Sample Preparation

The material investigated in this work is a semi-open/closed-cell polymer-based foam that was manufactured by D3O®. The variant under investigation is 'D3O® LITE D', which is advertised as a non-Newtonian shear-thickening material. To ensure consistency across strain-rates, a single sample size was used for both quasi-static and dynamic experiments. Common sample preparation techniques [1, 13] like the use of a hollow punch were initially adopted in this study. Other techniques for sample preparation were also pursued, including water-jet cutting and solid metal punch, but it was found that hollow punch technique results in the least amount of damage to the outer surface of the specimens. Using a special metallic hollow punch, disk samples of diameter 8 ± 0.3 mm were cut from an as-received sheet of uniform thickness of 4 mm, with the axis of the disk oriented along the through-thickness direction of the as-received sheet of foam. Care was taken to ensure that the samples'

end surfaces were parallel, and that minimum damage is induced to the edges during sample preparation. The choice of these sample size and shape resulted in constant strain-rate deformation and the best force equilibrium for the dynamic experiments, which are two criteria that are noted to be important and challenging when testing soft materials [21, 23–25] (results presented later in Figs. 6, 8).

The physical and mechanical properties provided by the manufacturer are listed in Table 1 [26]. The authors note that differences in the compressive strength between this study and those provided by the manufacturer is expected because the specimen sizes used in the ASTM D3575-14D is 25.4 mm × 25.4 mm × 25.4 mm, whereas the test specimen in our study is 8 mm in diameter and 4 mm in thickness (which is governed by the thickness of the as-received foam sheet). The sensitivity of material strengths to geometry and specimen-size effects are documented in the literature [1, 9], including experiences by other authors, and the authors expect that to manifest in differences in their strengths and those provided by the manufacture. Note, potential differences in composition, pore sizes and wall thicknesses may also occur as a consequence of different as-received sheet sizes.

Microstructure Characterization

For 2-D microstructure characterization, a Hitachi S-4800 field emission scanning electron microscope (SEM) was used. Figure 1a shows an SEM image of D3O® LITE D at ×100 magnification. From this cross-sectional view, the pores appear to be fairly circular and it is observed that the microstructure is mostly dominated by closed cells with small regions of semi-open cell features. These semi-open cells are noted with red circles in Fig. 1a, while the closed cells are more obvious. The concentrated bright features that appear near the cell wall boundaries, which lay inside the pore structures, are believed to be either small chunks of unexpanded polymer that remain intact during the cooling stage of manufacture process, or some form of additives that may have been introduced during the foaming process. Pore sizes were measured using ImageJ across the 10 SEM images (728 total pores), and were found to range between 50 and 200 μm with an average pore size of 82 ± 26 μm. Image processing techniques developed by Hogan et al. [27] were used to compute the area fraction of the pores as a measure of porosity. The average porosity of the material was found to be $83 \pm 5\%$ across the 10 images that were used this computation.

Next, shown in Fig. 1b is an SEM micrograph of the material taken at a higher magnification of ×600. Using

Table 1 Manufacturer's listed properties for D3O LITE D

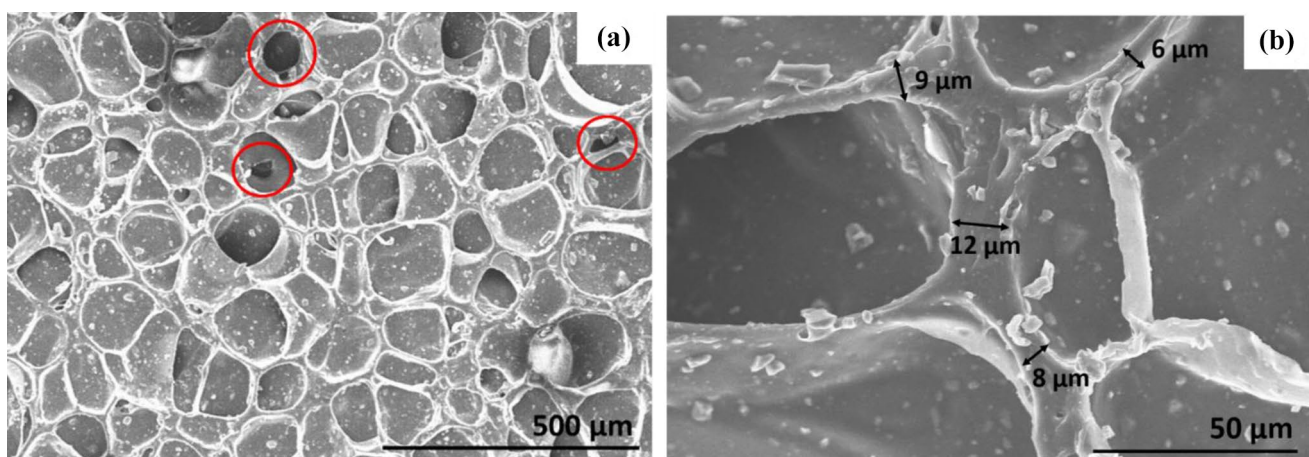| Material	Density range	Hardness	Tensile strength	Split tear strength	Compressive strength	Flexural modulus	Water absorbency
D3O lite D	200–220 Kg/m^3	60 Asker C	2.2 MPa	2.9 N/mm	190 kPa	5.59 MPa	1%
Test method	ISO 845: 2009	DTS004	ISO 1798: 2008	SATRA TM65	ASTM D3575-14D	DTS052	ISO 62: method 1

Fig. 1 **a** Scanning electron microscope (SEM) micrograph of D3O LITE D at ×100 magnification showing microstructure dominated by fairly circular pores of varying sizes with rare instances of semi-open pores represented by red circles. **b** SEM Micrograph at ×600 mag-nification showing sample wall thickness measurements. The bright features that are prominently visible in this cross-section are a result of additives/unexpanded bulk polymer. The length scales are denoted on the bottom-right corner. (Color figure online)

ImageJ, the wall thickness are computed across 10 images across the cross-section and wall thickness is estimated by measuring minimum thicknesses of the walls between adjacent pores. The average wall thickness across 10 images (750 total measurements) is calculated to be 8.3 ± 4.5 μm, with wall thicknesses ranging between 5 and 12 μm. Measurements of pore size and wall thickness are used later when describing the effect of microstructure on the rate-dependent failure this foam.

Experimental Methods

Quasi-Static Compression

The specimens were tested at a quasi-static strain rate of 0.04 s^{-1} using a Material Test System (MTS)—810 machine, a schematic of which is shown in Fig. 2 This assembly included visualization capabilities with a AOS PROMON U750—high-speed camera, which enabled us to observe macroscopic deformation features during testing. This camera has a resolution of 1280×1024 pixels and recorded at a framerate of 24 frames per second (FPS), which coincided with the data acquisition rate of the MTS machine. Both camera and MTS were triggered manually at the same time, and the synchronization was verified through comparison between when the piston displacement was first observed in the camera images with the displacement data recorded by the MTS machine (no adjustments were necessary). To
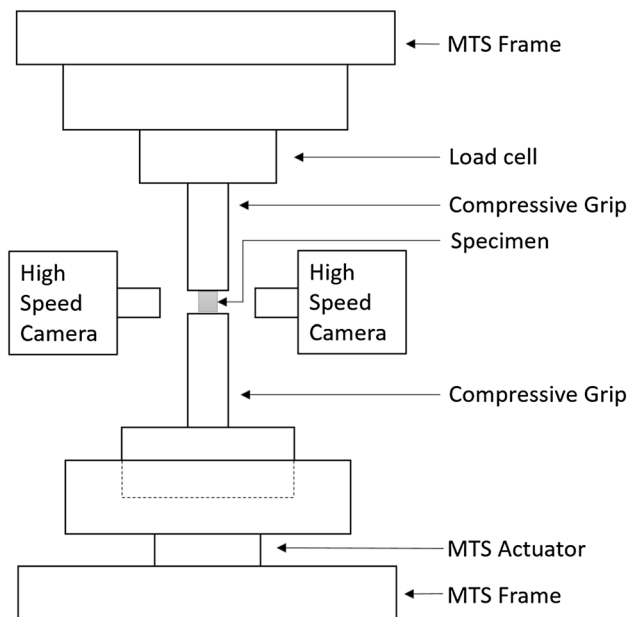
Fig. 2 Schematic diagram of the MTS experimental setup combined with two high-speed cameras perpendicular to each other facing the sample to aid in Poisson's ratio measurement

perform the test, the specimen is placed between a compressive grip of the MTS that consists of two 25.4 mm diameter steel bars (Fig. 2). These are guided and held with precise alignment. A cylindrical piston, moving at a constant displacement rate is used to compress the samples. A 10 kN load cell with a background noise corresponding to approximately ± 1 N recorded the time histories of the forces, and the displacement of the piston was measured to an accuracy of 0.001 mm using linear variable differential transformer (LVDT) displacement sensor. The actuator speed was set to 1 mm/min, corresponding to a nominal strain rate of 0.04 s^{-1} in the sample. Since almost no data regarding material densification was available before experimentation, the tests were terminated based on two conditions: first, when near-complete densification was observed in the force–displacement curve during loading, and second, when the actuator speed was no longer constant. Strains exceeding 90% were achieved in all the quasi-static trials. The engineering stresses are calculated by dividing the applied load by the original specimen surface area, and the engineering strains are computed by dividing the specimen displacement by the original specimen height. Three trials with same loading conditions were performed to verify repeatability of the material behavior.

High Strain-Rate Compression

The dynamic compression experiments were performed using a modified version of a SHPB apparatus [28], shown in Fig. 3. The setup consists of a gas gun, a striker bar, an incident bar, a transmission bar, sensors, a data acquisition system, and an ultra high-speed camera. In this study, the bars were made of solid aluminium with a density of 2700 kg/m^3 and stiffness of 68.9 GPa, which were procured from McMaster-Carr. Polymeric bars have also been used in past studies in the literature to study foams [29, 30], but are recognizably more challenging to manufacture. The use of aluminium pressure bars for testing soft materials has been well documented in literature [14, 17], and the authors have chosen to use them in their setup because they are more easily available and less expensive. In the dynamic tests, the polymeric foam sample is sandwiched between the incident and transmission bars, and the sample end faces were lubricated with high-pressure grease so as to reduce frictional effects and to allow for easy radial expansion during compression. This setup is consistent with others in the literature [1, 14, 29, 31].

In a SHPB experiment, a striker bar is launched from a pressurised gas gun and strikes the incident bar generating an elastic stress wave that travels through the incident bar to the sample, dynamically loading it. Due to mismatch of mechanical impedances of aluminium and the foam sample, reflected and transmitted waves are generated at the
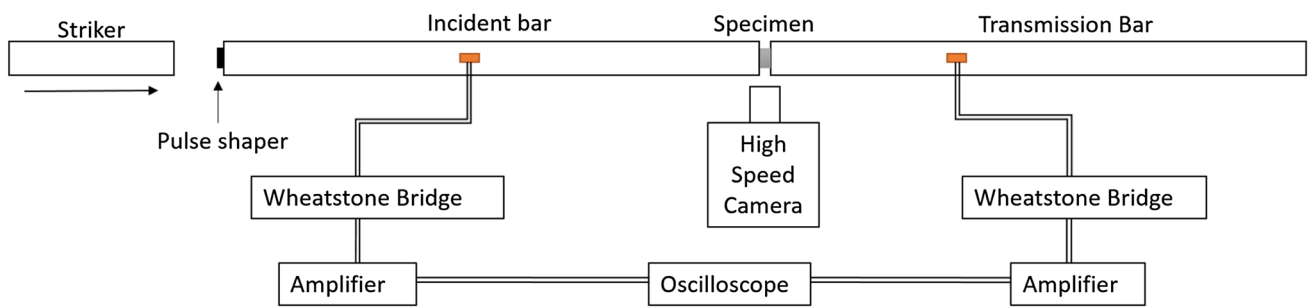
Fig. 3 Schematic diagram of the aluminium split Hopkinson pressure bar experimental setup combined with ultra-high speed camera for strain measurement and visualization of deformation features

left and the right interfaces of the sample, respectively. The transmitted wave travels through the sample into the transmission bar. The incident and reflected signals are recorded by a strain gage mounted on the incident bar and the transmitted signal is captured by a strain gage mounted on the transmission bar. The strain gages used in the setup in this study are $350\,\Omega \pm 0.3\%$ with a gage factor of $2.130 \pm 0.5\%$ (Micro Measurements CEA-13-250UN-350 semiconductor strain gages). The gages are connected to their individual conditional amplifiers (Vishay Inter-Technology 2310B) and a gain of 100–1000 is applied on the transmission gage because of the small magnitudes of transmitted stresses. The output from the conditional amplifier is fed to a Tektronix DPO2024B oscilloscope with 12-bit resolution recording at 500 MHz. Careful observation of transmitted gage raw voltage data in these experiments revealed a background noise approximately equal to ± 1 micro strain, which corresponds to 20% of the measured strain at the onset of yielding (~ 5 micro strain). The challenges of developing SHPB systems to measure the dynamic response of foams is widely documented [7, 13, 32, 33], and the approaches that the authors pursued are consistent with those in the literature. The lengths of projectile, incident bar and transmission bars are 500, 1000 and 910 mm respectively with a diameter of 12.7 mm. The length of the bars and the relative positioning of strain gages avoid overlapping of stress waves [20], also ensuring that longer loading durations are available in order to obtain large strains in the soft foam. To prevent a sudden impact from the striker against the incident bar and to achieve better force equilibrium and constant strain rate during testing, pulse shapers made of softer material than that of bar are to be used [7, 14]. Numerous pulse-shaping trials were performed using different combinations of materials. For example, copper discs of thicknesses of 0.1 and 1 mm, and different papers ranging from 100 to 240 GSM (Grams per Square Meter) were tested individually and in multiple combinations of each other. It was found that a 160 GSM paper pulse-shaper

generated the desired near-rectangular shape of the input pulse, which would ensure constant strain rate and best force equilibrium throughout the experiment.

To compute the stress–strain responses of the material, the theory of one-dimensional wave analysis in thin rods is used:

$$\sigma(t) = \frac{A_0}{2A_s} E_0 \left[\varepsilon_i(t) + \varepsilon_r(t) + \varepsilon_t(t) \right] \tag{1}$$

$$\varepsilon(t) = \frac{C_0}{L_s} \int_0^t \left[\varepsilon_i(t) - \varepsilon_r(t) - \varepsilon_t(t) \right] \tag{2}$$

$$\dot{\varepsilon}(t) = \frac{C_0}{L_s} \left[\varepsilon_i(t) - \varepsilon_r(t) - \varepsilon_t(t) \right] \tag{3}$$

where A_0 (m²) and A_s (m²) are the cross-sectional areas the bars and sample; $\varepsilon_i(t)$, $\varepsilon_r(t)$ and $\varepsilon_t(t)$ are the incident, reflected and the transmitted strain–time histories respectively; L_s (m) is the thickness of the sample; E_o (N/m²) is the Young's modulus of the bars and C_o (m/s) is the elastic bar wave speed which is given by

$$C_0 = \sqrt{\frac{E_0}{\rho_0}} \tag{4}$$

where ρ_0 (kg/m³) is the density of bar. Since the sample size is small, it can be assumed that the wave propagation effects within the specimen are negligible and this yields:

$$\varepsilon_i(t) + \varepsilon_r(t) = \varepsilon_t(t) \tag{5}$$

And Eqs. (1)–(3) are simplified to

$$\sigma(t) = \frac{A_0}{A_s} E_0 \varepsilon_t(t) \tag{6}$$

$$\varepsilon(t) = -2\frac{C_0}{L_s} \int_0^t \varepsilon_r(t) \tag{7}$$

$$\dot{\varepsilon}(t) = -2\frac{C_0}{L_s} \varepsilon_r(t) \tag{8}$$

To validate the working of the SHPB apparatus, it is necessary that dynamic stress equilibrium be attained in the samples [31] and this is verified by equating the forces at input bar–sample $[F_{S-I}(t)]$ and sample–transmission bar $[F_{I-T}(t)]$ interfaces, which are given by:

$$F_{S-I}(t) = A_0 E_0 [\varepsilon_i(t) + \varepsilon_r(t)] \tag{9}$$

$$F_{I-T}(t) = A_0 E_0 \varepsilon_t(t) \tag{10}$$

Shown in Fig. 4a is a force balance plot between forces calculated at the incident and transmitted ends of the sample. The vertical axis represents the force experienced in Newtons (N) and the horizontal axis represents time in microseconds (μs). The forces at the input bar–sample $[F_{S-I}(t)]$ and sample–transmission bar $[F_{I-T}(t)]$ interfaces are represented by black and brown curves, respectively. The overlapping of the curves indicate that reasonable dynamic force equilibrium is attained within the sample.

During testing, an ultrahigh-speed camera Shimadzu HPVX-2 was used to visualize deformation features, as well as to perform strain measurements. The camera is able to capture 256 images and is triggered by a split signal from the incident strain gage. In these experiments, the camera operated at a framerate of 1 million FPS at a resolution of 400×250 pixels. The camera was triggered from the incident strain gage and camera output pulses were used to correlate times between the images and the gage measurements. In the dynamic experiments, strain was measured by tracking overall displacements along edges of platens on either sides of the specimen. In each experiment, strain was tracked by tracking the displacement of two area markers on each side of the tested specimen, one on the incident bar and the other on the transmission bar which contained between 15 and 20 points, depending on

contrast and brightness of the area that was being tracked. This was done to more easily match the video images to the stress–strain curve in order to identify macroscopic deformation features that are observed in this material. Uncertainty of using the camera is approximated to lie within an error of one pixel where the initial sample size was measured to be 100 pixels in length, corresponding to a maximum strain uncertainty of 1%. A comparison of the strain rate versus time computed for one of the experiments using the wave equations (Eq. 8) and the rate versus time computed from tracking the displacements from the high-speed camera are shown in Fig. 4b. The horizontal axis represents time in microseconds and the vertical axis represents strain rate (s^{-1}). The green curve shows the unfiltered strain rate obtained from the wave equations and the blue curve represents the strain rate history achieved using the ultrahigh speed camera. The blue curve was plotted by taking the slope of the strain versus time, where the strain was measured using the ultra-high-speed camera. The global strain versus time was found linear throughout the entire event and so the strain rate is depicted linearly in Fig. 4b. The linearity is likely a result of not having enough resolution at corresponding framerates to measure minor variations in strain and strain rate. It was found that the strain rate calculated from the tracking technique lied within 3% error of the rate calculated from the wave equations for any given time after stress equilibrium has been obtained (i.e. at strains greater than 8%). Finally, three tests with same loading conditions were performed to verify repeatability of the experiments and it was found that with the same cylinder pressure, there was a variability of ~5% in the projectile velocity, which caused a variability in strain rates of 5284–5720 s^{-1}.
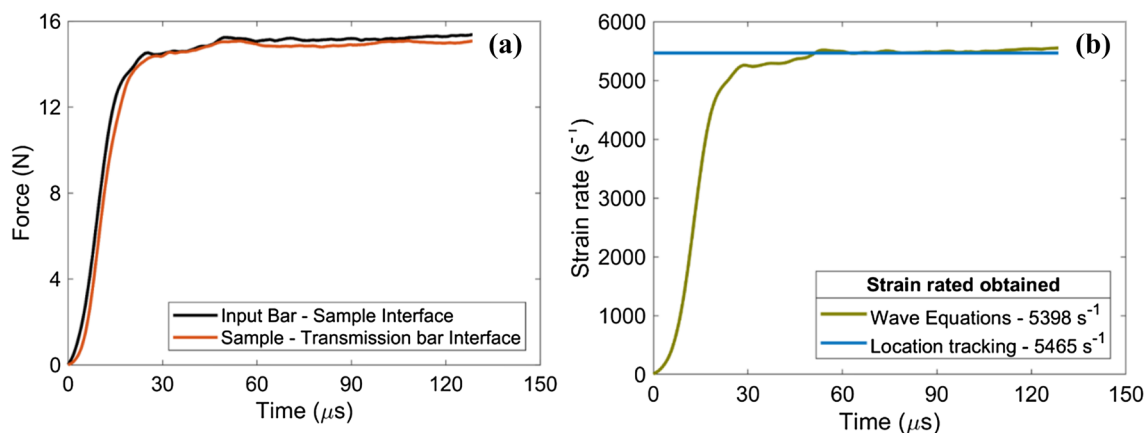

Fig. 4 **a** Plot showing dynamic force balance between foam sample's end surfaces during dynamic compressing testing using split Hopkinson pressure bar. **b** Strain rate history of the sample observed during dynamic compression using wave equations, and using location tracking technique which tracks markers on ultra-high speed camera images to calculate strain and strain rate. Both based on individual MATLAB programs

Experimental Results

Shown in Fig. 5 is a plot of the quasi-static and dynamic stress–strain curves of the D3O LITE D, including multiple curves for experimental variability. The x-axis denotes the absolute strain and the y-axis depicts stress in log scale. The points 1–8 included on one example quasi-static and one example dynamic curve correspond to high-speed camera images that are shown and discussed later in Figs. 6 and 8. The strains for which images are selected are different for the quasi-static and dynamic cases. For the quasi-static case, strains are selected at transitional points on the stress–strain curve, as well as those strains that correspond to the onset or evolution of notable deformation features in the images. Similarly for the dynamic experiments, image locations are selected to best visualize the onset and evolution of deformation features for the higher strain rate. The results for both quasi-static and dynamic strain rates are discussed in greater detail subsequently.

Quasi-Static Regime

It is observed that the compressive response of the material in the quasi-static regime exhibits a typical elastomeric foam behavior with a few notable exceptions. Namely, typical foam responses have a sudden change in slope when the stress reaches elastic stress limit σ_{el}^* and its value is easily identifiable. However, in this material, it was found that there was a gradual transition from the elastic regime to the plateau regime beginning at a strain of 2% and plateauing at approximately 6% strain, which does not yield a specific value of σ_{el}^*. Therefore, average stress over the specified strain range between 4.6 to 5.2% was calculated, where an initial increase in slope is observed, and σ_{el}^* was measured to be 120 ± 55 kPa over this range. In the figure, the curve then starts to plateau at around 6% at a stress of about 145 kPa, indicating the start of post-elastic collapse regime. From this point, the sample continues to harden with a linearly increasing hardening rate until a strain of ~60% is reached within the sample. The sample then starts to densify at an increasing rate until a strain of ~83% at a stress of 5.05 ± 2.1 MPa is reached in the sample, at which point the sample starts to densify rapidly. It is also observed that

Fig. 5 Stress–strain curves from quasi-static and dynamic compression experiments. Black points on the quasi-static curve are represented by high-speed camera images in Fig. 6; red points on the dynamic curve are represented by ultra-high speed camera images in Fig. 8. (Color figure online)
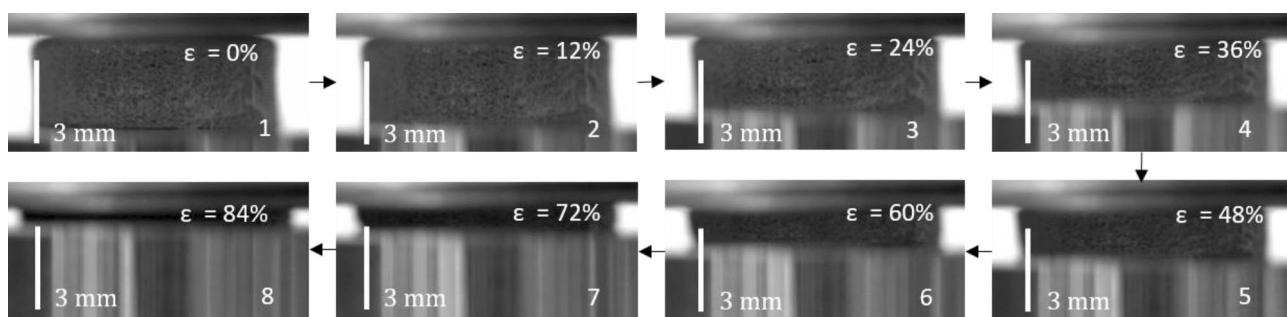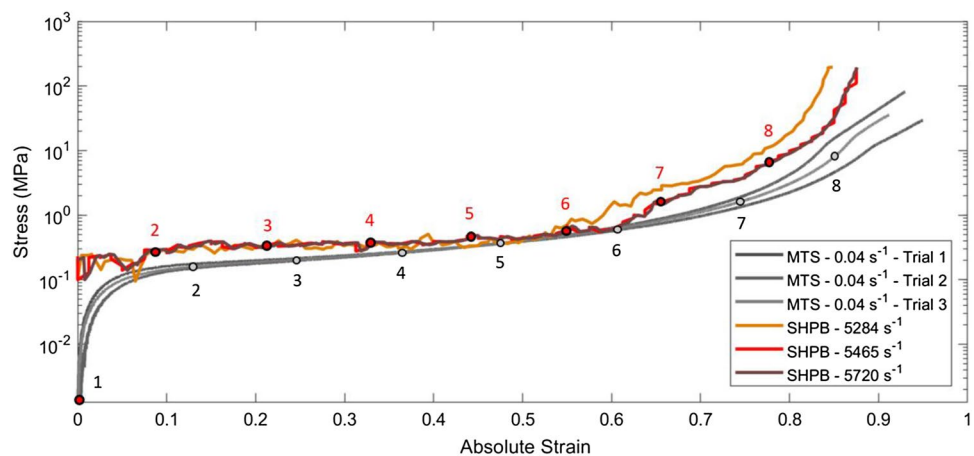

Fig. 6 Time-evolved quasi-static compression failure of the D3O foam at 0.04 s^{-1} using MTS 810 apparatus. Inter-frame strains are denoted at the top-right corner of each image and specimen length scales are denoted on the bottom-left corner of each image. Large-scale linear deformations are not observed in the quasi-static case, like the dynamic case

Fig. 7 Plot showing effect of different filtering levels on stress magnitudes and global trends of dynamic compressive response of D3O LITE D foam. The red curve is indicative of acceptable filtering level with a strain segment size of 0.2%. The light grey and dark grey are example curves at larger segment sizes of 0.5% and 1% respectively, that show distortions from original response indicating over-filtering. (Color figure online)
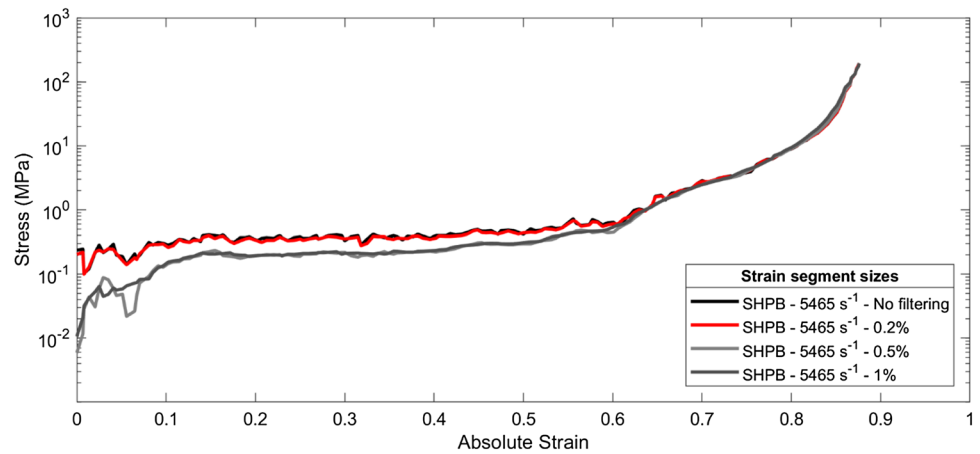

Fig. 8 Time-evolved dynamic compression failure of the D3O at 5465 s⁻¹ using split Hopkinson pressure bar apparatus. Inter-frame strains are denoted at the bottom-left corner of each image and specimen length scales are denoted on the top-right corner of each image. The red lines in image 3 emphasize larger-scale vertical localization bands that start to form in this material at approximately 10% strain. This corresponds to log-linear region in the red line in Fig. 5. (Color figure online)
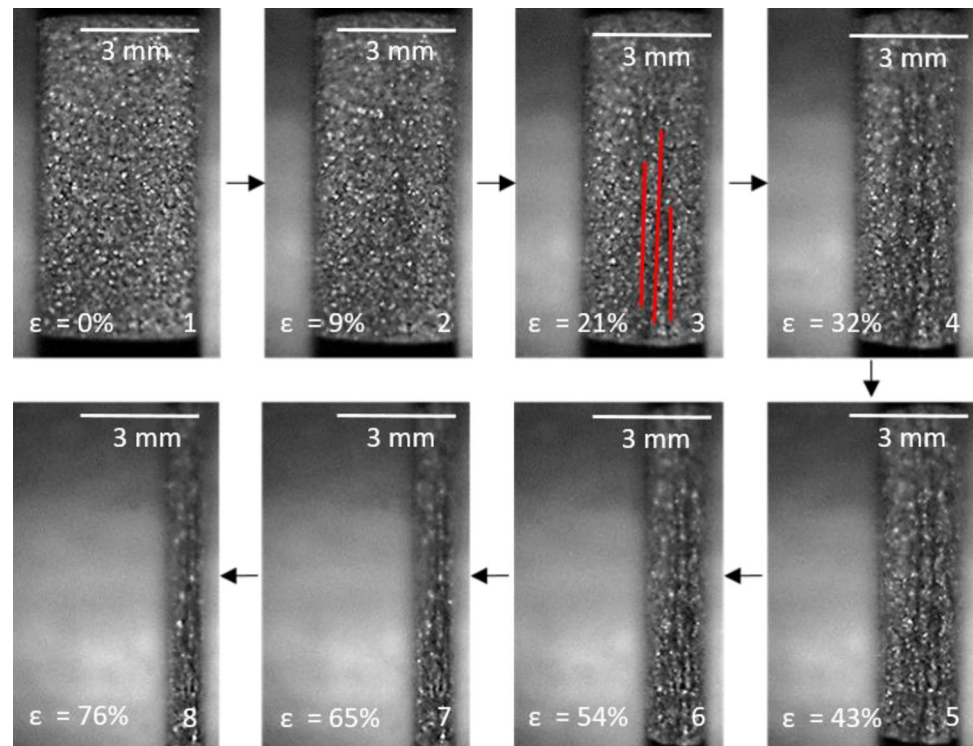
there was a sudden increase followed by a gradual decrease in the hardening rate at this strain. The strain of ∼83% coincides with the porosity of the material, and so this hardening behavior likely corresponds to near-complete pore collapse. At this point, the porosity is completely crushed out and the foam tends to behave linearly like the elastic part of the compressive behaviour of the parent bulk polymer [11, 13]. To understand the variability in the material behavior and consistency of the mechanical properties obtained from the experiments, three stress–strain curves under the same strain-rate and loading conditions were obtained, and these are also shown in Fig. 5. It can be seen that below strains of 70%, the stress–strain curves overlap within 4% error, and the variability observed after 70% strain are related to

the differences in material composition, individual sample density and microstructure. For a given sample, the pore collapse strain ranges between 114 and 126 kPa, while the stress variability at 90% strain can range between 28 and 44 MPa.

To better understand the failure mechanisms that influence the stress–strain responses, images taking using a high-speed camera during quasi-static testing (Fig. 6) are presented. The image numbers correspond to the numbers shown on the quasi-static stress–strain curves in Fig. 5. Image 1 shows the start of the experiment at 0% strain, and is shown for reference. From image 2, it is observed that from a strain of 0–12%, there is a small noticeable lateral deformation. This suggests that the Poisson's ratio may be

negligible throughout the elastic regime and early plateau. This is consistent with observations by Liu et al. [29] for their polymeric foam (acquired from Airbus). As seen from images 3 through 6, very low lateral deformation is observed corresponding to a Poisson's ratios less than 0.01; no clear deformation features are visible on the material surface. In image 7, visually distinguishable deformation appears in lateral direction at a strain of ~72%, and densification begins to occur ending the plateau regime. Finally, image 8 is taken at a strain of ~84%, where considerable lateral expansion is observed and at strains higher than this, the sample moves out of the camera's field of focus. All of lateral deformation measurements were performed using ImageJ. Given that the specimen is cylindrical, it was assumed that transverse strain observed is uniform. The transverse strain was calculated by measuring the radial expansion of the specimen by estimating the diameter using the line function in ImageJ. These diametrical changes were measured using the tangent equation following convention [34]. This was done at five equidistant locations across the thickness at specific strain intervals and transverse strain is averaged. Poisson's ratio was calculated by taking the ratio of transverse strain to the longitudinal strain. Throughout the range of strains, it was observed that there were no distinctive macroscopic deformation features on the imaged surface, which are contrasted with dynamic results next.

Dynamic Regime

Prior to discussing the stress–strain responses for the dynamic experiments in Fig. 5, the authors first discuss the effect of filtering levels on the strain–strain curves presented in Fig. 7. In our experiments, data from the oscilloscope was sampled at 500 MHz (fixed oscilloscope setting), and filtering techniques were explored to better visualize the raw data and contrast it with the quasi-static experimental trends (e.g., features like the elastic collapse, densification). Some level of filtering of high strain-rate data appears to be frequently used in the published literature on foams [1, 7, 13, 14] (based on smoothness of curves), with limited discussion for filtering approaches (e.g., frequency-based filters [10]). To explore the effect filtering, the authors use a first order Savitzky–Golay (SG) filter in Matlab, which helps increase the signal-to-noise ratio without greatly distorting the signal. The smoothing is achieved using a process called convolution, which fits segments of adjacent data points with a low-degree polynomial by the method of linear least squares. The choice of this filter, which the authors believe, allows maintaining the general trends and stress magnitudes in the data (which the authors explore here). In this exercise, the authors show the effect of different filtering levels for one of the dynamic experiments in Fig. 7. Here, the authors selected to apply filtering levels beginning at filtering segment sizes

corresponding to 0.05% strain and increasing by 0.05% strain up to 1%, which the authors believed to represent low degrees of filtering when first selected. The figure shows an unfiltered curve, and curves for filtering levels for segment sizes of 0.2% (corresponding to 180 points), 0.5% (corresponding to 450 points), and 1% (corresponding to 900 points). The black curve shows the unfiltered data, followed by the red curve which corresponds to a segment size of 0.2% strain. It can be seen that the red curve overlaps over the black curve in all ranges of strain suggesting that both magnitudes and trends are preserved at this level of filtering. Increasing the strain segment size to 0.5% strain leads to a three fold reduction in elastic collapse stress, as well localized distortion of the general trend at low strains which are represented by the light grey curve. The dark grey curve represents filtering corresponding to a strain segment size of 1% and it can be observed the overall trend is captured but stress magnitudes are reduced drastically with increasing segment sizes. These values demonstrate the outcome of the analysis. Namely, it was observed that increasing the strain segment size to greater than 0.25% strain leads to distortions of the general trend and decreased stress magnitudes, and so a size of 0.2% strain was selected because this lied within acceptable filtering levels.

Now that filtering has been explored, the authors return to describe the stress–strain response of the foam in Fig. 5 for strain rate of 5284–5720 s^{-1}. For the dynamic case, the linear-elastic regime spans up to a strain of ~1% and the elastic collapse stress σ_{el}^* is calculated to be approximately equal to 243 ± 47 kPa. In our experiments, the transition from the elastic regime to the plateau regime begins at a strain of 0.8% and plateaus at around 1.5% strain. The authors note here that the stress in the sample has not yet equilibrated (see Fig. 4a), and care should be given to interpretation of these values as discussed in Song et al. [7]. In our tests, a constant strain rate and force balance is achieved in the sample at ~8%. In the dynamic tests, the stress in the sample continues to rise between 8% (stress of 280 ± 25 kPa) and 45% (460 ± 40 kPa) at a constant rate in this log-linear representation. This linear rise corresponds to an initial plateau regime. Interestingly, there is a secondary hardening regime beyond 45% strain that increases logarithmically until a strain of 81–83% (22.5 ± 4.0 MPa). This pronounced hardening rate corresponds to densification of the foam sample. Again, this likely corresponds to pore collapse in the sample, albeit at a slightly less strain value than observed in the quasi-static experiments. After this point, there is an inflection in the curve at ~83%, which is believed to correspond to complete densification. After a strain of ~81% is achieved within the sample, the material hardens more rapidly than the quasi-static tests, and this likely corresponds the behavior of the parent material.

To better understand the hardening regimes, ultra-high-speed camera images taken during deformation (Fig. 8) are presented. In this D3O LITE D foam, some unique macroscopic deformation features are observed. Shown in Image 1 of Fig. 8 is a reference image taken at 0% strain for the dynamic experiments. Image 2 corresponds to strains of around 8–10%, where small band-like features begin to appear. Image 3 shows the sample at 18–20% strains where these features become more visually apparent as indicated by the red lines in the image. Note the red lines are used to highlight the location of these vertical bands and this meant to ease the reader in visualizing the growth of the bands in subsequent images. These band-like deformation features are termed as "localizations" hereafter. It was observed that at strains between 20–35% (Image 4), a greater number of localization features appear to nucleate, and this corresponds to the near-horizontal plateau in the log-linear regime of the stress–strain curve in Fig. 5. These localization features continue to nucleate and grow perpendicular to the compressive loading direction until strains of 42–45% are reached within the sample, shown in image 5. After 45% strain, no more new nucleations are observed in the ultra-high-speed camera images, and at strains beyond 45%, the localizations begin to coalesce with each other until they span the entire length of the sample at 75–80% strain (shown in images 6–8). In the dynamic experiments, lateral expansion was measured at the aforementioned strains using ImageJ and a constant expansion rate was observed leading to a Poisson's ratio of ~0.11. After strains of 85–90% are reached, the sample expands out of the field of focus of the camera.

Discussion

This paper investigated the compressive failure of a shear-thickening polymeric foam for quasi-static and dynamic conditions. It is important to better understand the behavior of these materials since this class of foams are currently being employed in energy absorption equipment (e.g., helmet liners for US team sports such as football, baseball and ice hockey, as well as protective inserts for motorcycle jackets) and also in some military applications [35]. Limited data on these materials, and shear thickening foams in general, exist in the literature, and so the authors believe that this paper makes contributions towards better understanding how microstructural features and lengths scales of these types of foams may be related to quasi-static and dynamic compressive failure. In what follows, the authors discuss the results of this foam in the context of their general understanding of how polymeric foams behave.

To summarize the results and discussion of this paper, Table 2 is presented which consists of the stress regimes, Poisson's ratio measurements (ν) and the dominating failure mechanisms corresponding to that given ranges of strains. This table also provides image numbers corresponding to images from high speed camera for quasi-static case, and similarly for ultra-high speed camera images for the dynamic case from Figs. 6 and 8 respectively, so that it is easier for the reader to visualize camera images while referring to the table.

Table 2 Summary table showing the stress regime, Poisson's ratio (ν) and the dominating failure mechanism corresponding to the given ranges of strains

Strain range	Quasi-static				Dynamic				
	#	Stress regime	υ	Failure mechanism	#	Stress regime	υ	Failure mechanism	Deformation features
0–10	1	Linear elastic	0.064	Elastic collapse	1	Linear elastic	0.095	Elastic collapse	None
10–20	2	Plateau	0.064	Buckling	2	First plateau	0.095	Buckling	Nucleations begin
20–30	3	Plateau	0.075	Buckling	3	First plateau	0.061	Cell wall bending	Higher nucleations
30–40	4	Linear hardening	0.042	Cell wall bending	4	First plateau	0.089	Cell wall bending	Nucleations stop
40–50	5	Linear hardening	0.064	Cell wall bending	5	Secondary hardening	0.089	Pore collapse	Localizations grow
50–60	6	Linear hardening	0.053	Pore collapse	6	Secondary hardening	0.100	Pore collapse	Growth & coalescence
60–70	6	Densification	0.204	Pore collapse	7	Densification	0.122	Tearing	Growth & coalescence
70–80	7	Densification	0.569	Tearing	8	Densification	0.111	Complete pore collapse	Full sample length
80–90	8	Complete densification	-	Complete densification	-	Complete densification	-	Post-pore collapse	-

It is to be noted that each failure mechanism, once activated continues to remain active until failure. Also, image numbers corresponding to that of Fig. 6 are provided for high speed camera images for quasi-static case, and similarly for ultra-high speed camera images for the dynamic case with respect to Fig. 8

First, the authors correlate commonly known deformation mechanisms to the stress–strain curves of our D3O LITE D foam in quasi-static and dynamic conditions (Fig. 5). Generally, three different phases of deformation are observed during compressive failure of polymeric foams [6, 8, 13]. The first phase is linear-elastic regime, where the stress–strain response follows Hooke's law and the strain is completely recoverable. For polymeric foams, the linear-elastic limit is limited to small strains, typically less than 5% strain [1, 7]. It is to be noted that elastomeric foams can undergo much higher strains than these and the deformation can still be mostly recoverable, but is non-linear [8]. The second phase is characterized by non-linear elasticity, where the material continues to plateau at a relatively constant stress, known as the elastic collapse stress σ_{el}^*. This property of foams is exploited for energy-absorbing applications [6]. The third and final phase of deformation is known as densification, where the foam begins to respond like a compacted solid [1, 13]. For semi-closed cell foams, these deformation and failure mechanisms are usually more complicated than fully open or closed celled foams due to the presence of higher number of face edges where damage can nucleate [10]. Each of the three phases is explained in the context of our material hereafter with a main focus on dynamic response.

In our dynamic experiments, the linear elastic regime extends to about 1–1.5% strain and in this regime all stresses are carried by only the cell ligaments, which show small regions of buckling, directly contributing towards the stiffness of the material. There is no failure in the linear elastic regime and the strains are fully recoverable. Similar mechanisms are observed in the quasi-static case as well, but at different elastic strain limits as discussed earlier. In our dynamic experiments, the post-elastic collapse behaviour begins at around 1.5% strain and is dominated by buckling of both cell edges and faces. This mechanism spans the entire inelastic regime. In the first plateau, permanent bending of cell walls dominates up to a strain of ~45% alongside large-sized buckling regions near the cell walls. In the second plateau region following the permanent deformation of the cell walls, the cell faces begin to rupture followed by tearing of the cell edges at strains of ~62%, and this process occurs progressively in the rest of the plateau regime. Initial damage is observed at the near-closed cells, and these cells begin to rupture at the strain nearing the end of plateau, reaching to the point of densification, which begins at around 81% strain. In our quasi-static experiments, the post-elastic collapse behaviour begins at ~6% strain and hardens linearly until ~60% strain after which gradual densification is observed up to strains of ~83%. Similar failure mechanisms that have been discussed for dynamic conditions are activated in quasi-static conditions at similar strains except for that of complete densification. A deviation from typical foam behaviour [6, 8, 11, 13, 19, 36] in our experiments was

that the hardening rate of the plateau stress was found to be more than an order of magnitude higher than the elastic collapse stress in quasi-static rate and almost two orders of magnitude higher in dynamic strain rate conditions. At these high strains, the opposing cell walls have been observed [13] to crush together and cell wall material is itself compressed and complete densification is observed. It is to be noted that each failure mechanism, once activated continues to remain active until failure.

After densification, complete pore collapse is observed. In the quasi-static case for our experiments (Fig. 5), there was an inflection at the curve around $87 \pm 3\%$, and the authors believe that is likely related to complete pore collapse. In the dynamic case, the inflection was observed around $83 \pm 3\%$, which was lower than the quasi-static. The formation of the structural-scale vertical localizations are believed to be responsible for the lower pore collapse strain in the dynamic case as a result of these localization features consuming porosity during their nucleation, growth, and coalescence. This factor needs to be considered in any dynamic failure modelling of foams where large strains at high strain rates are experienced because the formation of these localizations govern the hardening rates in the plateau regime, which in turn are responsible for material response at high strain rates. Lastly, after complete pore collapse, post pore collapse hardening was observed. Post pore collapse hardening rates in both quasi-static and dynamic cases are found to be greater than the rate of densification in their respective cases. The dynamic post pore collapse hardening rate is observed to be greater than the quasi-static post pore collapse hardening rate. This is explained by the general rate dependency behaviour in bulk polymers [14] at high strains given when the entire porosity in the foam is crushed out, the sample essentially behaves like a bulk polymer material. Although not explicitly reported by the authors, similar effects are observed in other materials [8, 13]. After this point, at very large compressive strains of over 85%, the sample under the given mechanical loading tends to behave like material response of the parent material. It is to be noted that the vertical axis shown in Fig. 5 is of log scale and these hardening rates may not be as easily visualized in the stress–strain curves presented in the paper.

The localization behavior foams advertised as shear thickening is not currently understood, but is likely related to some combination of chemical composition and structure (held proprietary by the manufacturer), the microstructure (in terms of pore size and wall thickness), and the strain energy that is available for failure (assessed via mechanical testing and stress–strain response). Additional experiments are needed to better understand the mechanisms for nucleation and growth of the localization features (e.g., interrupted compression or impact experiments coupled to X-Ray imaging of internal microstructure features), and energy-based or

computational models are required to confirm experimental observations.

With this in mind, the authors briefly explore potential reasons for the observed localization features in this foam, which, to the knowledge of the authors, are unique to this as-advertised shear thickening foam. As mentioned, these localization features are believed to be a consequence of chemical composition and structure, and the microstructure (i.e., in terms of pore size and wall thickness). In this discussion, the authors focus on the microstructural contributions since the chemical composition, structure information and foam manufacturing processes are proprietarily held by the manufacturer. The authors link the localization features to instabilities that lead to buckling of cell walls perpendicular to the compressive loading direction. The onset of these instabilities are believed to be related to the relative sizes of the pores and the wall thickness, where relatively large pore sizes results in relatively higher localized stresses concentrations, and relatively thinner walls are more susceptible to collapse under these relatively higher stresses. In this D3O LITE D material, the ratio of pore sizes (average of 82 ± 26 μm) to wall thickness (average of 8.3 ± 4.5 μm) is 4.3 to 28 (average 9.8). In other materials, where SEM images are available, the authors observe wall thickness to pore sizes ratios of ~ 0.025 and ~ 0.002 [18, 24], and perhaps these ratios play a role in the unique behavior of the Lite D foam. It is, however, to be noted that these materials have different compositions, and this form of foam microstructure with its unique wall thickness to pore size ratio, pore shapes, distributions, and locations of unexpanded polymer is found to be unique to D3O LITE D when compared to other images of foam microstructures in literature [1, 9–11].

Conclusion

The compressive response of D3O LITE D dilatant foams under quasi-static strain rate of 0.04 s^{-1} and dynamic strain rate of 5284 to 5720 s^{-1} has been studied. Experimental methods for characterizing and studying the dynamic response of foams have been established and have found to reconcile with traditional experimental techniques. Comprehensive insights into compressive behavior of shear thickening foams are provided, which is relatively an unexplored area of research despite current use of these materials in many applications. Most notably, under dynamic loading conditions, unique macroscopic localization features are observed in the D3O LITE D foam under investigation in this paper, which do not appear at quasi-static rates or in any high rate testing of other polymeric foams (to the knowledge of the authors). This data can be used for modelling the observed localizations as a unique failure mechanism in mechanism-based modelling approach to predict

material response. More studies at intermediate strain rates are required to identify the threshold strain rate for these localizations and to study the effect of these localizations on shear thickening behavior. As this is the first time that the D3O LITE D foams have been characterized in this way, the authors believe these experimental results will also serve as a good starting point for impactful modelling [9, 36]. The results of the tests performed and the future tests will be put together to make models to predict the effect of microstructure, strain rate and localizations on the compressive response of shear thickening foams.

References

1. Ouellet S, Cronin DS, Moulton J, Petel OE (2013) High rate characterization of polymeric closed-cell foams: challenges related to size effects. In: Zimmerman KB (ed) Conference proceedings of the society for experimental mechanics series, vol 1. Springer, New York, pp 21–28
2. Nemat-Nasser S, Kang WJ, McGee JD, Guo WG, Isaacs JB (2007) Experimental investigation of energy-absorption characteristics of components of sandwich structures. Int J Impact Eng 34(6):1119–1146
3. Sounik DF, Gansen P, Clemons JL, Liddle JW (1997) Head-impact testing of polyurethane energy-absorbing (EA) foams. SAE Trans 106:211–220
4. Cernak I, Merkle AC, Koliatsos VE, Bilik JM, Luong QT, Mahota TM et al (2011) The pathobiology of blast injuries and blast-induced neurotrauma as identified using a new experimental model of injury in mice. Neurobiol Dis 41:538–551
5. Kiernan S, Cui L, Gilchrist M (2009) Novel energy absorbing materials with applications in helmeted head. University College Dublin, Dublin, pp 1–4
6. Di Landro L, Sala G, Olivieri D (2002) Deformation mechanisms and energy absorption of polystyrene foams for protective helmets. Polym Test 21(2):217–228
7. Song B, Chen WW, Dou S, Winfree NA, Kang JH (2005) Strain-rate effects on elastic and early cell-collapse responses of a polystyrene foam. Int J Impact Eng 31(5):509–521
8. Cronin DS, Ouellet S (2016) Low density polyethylene, expanded polystyrene and expanded polypropylene: strain rate and size effects on mechanical properties. Polym Test 53:40–50
9. Bouix R, Viot P, Lataillade JL (2009) Polypropylene foam behaviour under dynamic loadings: strain rate, density and microstructure effects. Int J Impact Eng 36(2):329–342

10. Gao K, van Dommelen JAW, Geers MGD (2016) Microstructure characterization and homogenization of acoustic polyurethane foams: Measurements and simulations. Int J Solids Struct 100–101:536–546

11. Saha MC, Mahfuz H, Chakravarty UK, Uddin M, Kabir E, Jeelani S (2005) Effect of density, microstructure, and strain rate on compression behavior of polymeric foams. Mater Sci Eng A 406:328–336

12. Marais ST, Tait RB, Cloete TJ, Nurick GN (2004) Material testing at high strain rate using the split hopkinson pressure bar. Latin Am J Solids Struct 1:219–339

13. Ouellet S, Cronin D, Worswick M (2006) Compressive response of polymeric foams under quasi-static, medium and high strain rate conditions. Polym Test 25(6):731–743

14. Chen W, Lu F, Cheng M (2002) Tension and compression tests of two polymers under quasi-static and dynamic loading. Polym Test 21:113–121

15. Wang L, Labibes K, Azari Z, Pluvinage G (1994) Generalization of split Hopkinson bar technique to use viscoelastic bars. Int J Impact Eng 15(5):669–686

16. Santa Maria JA, Schultz BF, Ferguson JB, Gupta N, Rohatgi PK (2014) Effect of hollow sphere size and size distribution on the quasi-static and high strain rate compressive properties of Al-A380-Al2O3 syntactic foams. J Mater Sci 49(3):1267–1278

17. Chen W, Zhou B (1998) Constitutive behavior of epon 828/T-403 at various strain rates. Mech Time-Depend Mater 2:103–111

18. Viot P, Beani F (2003) Comportement de mousses polyme`res en compression dyna-mique. Revue des Composites et des Mate´riaux Avance´s 13(3):283–292

19. Avalle M, Belingardi G, Montanini R (2001) Characterization of polymeric structural foams under compressive impact loading by means of energy-absorption diagram. Int J Impact Eng 25(5):455–472

20. Gary GT (2000) Classic split-Hopkinson pressure bar testing. In: Kuhn H, Medlin D (eds) Mechanical testing and evaluation, metals handbook, vol 8. American Society for Metals, Materials Park, pp 462–476

21. Gray GT III, Blumenthal W (2000) Split Hopkinson pressure bar testing of soft materials. In: Kuhn H, Medlin D (eds) ASM handbook, mechanical testing and evaluation, vol 8. ASM International, Materials Park, pp 488–496

22. Subhash G, Liu Q, Gao XL (2006) Quasistatic and high strain rate uniaxial compressive response of polymeric structural foams. Int J Impact Eng 32(7):1113–1126

23. Clamroth R (1981) Determination of viscoelastic properties by dynamic testing. Polym Test 2:263–286

24. Harris JA (1987) Dynamic testing under nonsinusoidasl conditions and the consequences of nonlinearity for service performance. Rubber Chem Technol 60:870–887

25. Meyers MA (1994) Dynamic behavior of materials. Wiley, New York

26. D3O.com (2018) D3O® LITE SHEET [online]. Available at: https://www.d3o.com/wp-content/uploads/2016/10/D3O-LITE-SHEET-V2.pdf. Accessed 17 Sept 2018

27. Hogan JD, Farbaniec L, Daphalapurkar N, Ramesh KT. On compressive brittle fragmentation. J Am Ceram Soc 99(6):2159–2169

28. Kolsky H (1949) An investigation of the mechanical properties of materials at very high rates of loading. Proc Phys Soc 62:676–700

29. Liu J, Saletti D, Pattofatto S, Zhao H (2014) Impact testing of polymeric foam using Hopkinson bars and digital image analysis. Polym Test 36:101–109

30. Liu Q, Subhash G (2006) Characterization of viscoelastic properties of polymer bar using iterative deconvolution in the time domain. Mech Mater 38(12):1105–1117

31. Irausquín I, Pérez-Castellanos JL, Miranda V, Teixeira-Dias F (2013) Evaluation of the effect of the strain rate on the compressive response of a closed-cell aluminium foam using the split Hopkinson pressure bar test. Mater Des 47:698–705

32. Chen W, Song B (2011) Split Hopkinson (Kolsky) bar. Mechanical Engineering Series. Springer, New York

33. Song B, Chen W (2005) Split Hopkinson pressure bar techniques for characterizing soft materials. Lat Am J Solids Struct 2(2):113–152

34. Sanborn B, Song B (2018) Poisson's ratio of a hyperelastic foam under quasi-static and dynamic loading. Int J Impact Eng. https://doi.org/10.1016/j.ijimpeng.2018.06.001

35. D3O.com (2018) Defense [online]. Available at: https://www.d3o.com/defence/. Accessed 17 Sept 2018

36. Avalle M, Belingardi G, Ibba A (2007) Mechanical models of cellular solids: parameters identification from experimental tests. Int J Impact Eng 34(1):3–27